Journal of the Australian Ceramic Society (2022) 58:217–225
https://doi.org/10.1007/s41779-021-00684-0

RESEARCH

Electrochemical performance of the Mn-doped CeO_2: nanoparticles for sensitive electrocatalysts the urea concentrations

Anees A. Ansari[1] · **Manawwer Alam**[2]

Received: 28 February 2021 / Revised: 1 October 2021 / Accepted: 14 November 2021 / Published online: 23 November 2021

Abstract

Manganese-substituted cerium oxide nanoparticles (CeO_2:Mn NPs) were successfully prepared by the polyol-based co-precipitation method, and applied for construction of an electrocatalytic electrode. The crystallographic structure, phase purity, and morphological characteristics were examined by X-ray diffraction (XRD) and transmission electron microscopy (TEM) procedures. XRD results indicate a cube shape with an average crystalline size of ~ 10 nm. EDX analysis verified the homogeneous mixing of substitution of Mn ion in CeO_2 crystal lattice. UV/visible spectrum and bandgap energy (3.27 eV) were observed to confirm the phase formation and optical properties of the material. Cyclic voltammetry (CV) and electrochemical impedance spectroscopy (EIS) tools were applied to inspect the electrochemical properties of the material. Both applied electrochemical methods verified the excellent electroactive surface area and electrocatalytic behavior of the constructed CeO_2:Mn/glassy carbon electrode (GCE). The high sensitivity, strong reproducibility, and promising stability were also observed by the electrode on changing the potential scan rate. More significantly, in the catalyze or detection of the target analyte (urea), adequate recoveries were obtained for the evolved electrocatalyst/sensor, which showed a wide prospect of practical use. The high electrocatalytic activity of the CeO_2:Mn/GCE model in the concentration range (3.90–1000 mg/dl) catalysts was the synergistic relationship between Mn and CeO_2 NPs. This CeO_2:Mn matrix could be an effective strategy to electro-catalyze various hazardous analytes (chemicals) such as catechol, phenol, and industrial effluents.

Keywords Manganese · Cerium oxide · Electrocatalysts · Urea · Cyclic voltammetry

Introduction

Currently, sensors/biosensors are an important engineered miniaturized device that uses a chemical/biological element for signal detection (enzyme, hazardous chemicals, antibody, proteins, nucleic acid, and oligonucleotides/DNA) as a sensing system combined with a transducer [1–8]. A sensor uses the chemical/biomolecule selectivity and processing capacity of modern microelectronics and optoelectronics and is thus a versatile analytical device for clinical, industrial, and medical diagnostics and other applications [3, 5, 9, 10]. Recently, the most widely applied class of sensors is electrochemical sensors/biosensors [5, 7, 10–14]. These are focused on the fact that electrochemical species such as electrons are absorbed or produced during a chemical/bio-interaction phase, which generates an electrochemical signal that can be determined by an electrochemical detecting device. In sensing applications, electrochemical sensors/biosensors have been most extensively recognized. These sensors/biosensors can be used in turbid media and have shown similar instrumental sensitivity and are more likely to be miniaturized [7, 14, 15]. Potentiometry and amperometry are commonly used to base electrochemical biosensors. Electrochemical biosensors can further be split into conductometric, potentiometric, and amperometric biosensors, based on the electrochemical property to be calculated by a detector device. These electrochemical sensors are expected to be considered a vital part of both biochemical and clinical applications because of their precision, transportability, fast response time, ease of operation, and economical. The predominant miniaturization tools allow multiple microscopic electrodes to be packed together with transducers into a tiny biochip system footprint, resulting in the design of high-density bio-arrays.

✉ Anees A. Ansari
amustaqeemahmad@ksu.edu.sa; aneesaansari@gmail.com

[1] King Abdullah Institute for Nanotechnology, King Saud University, Riyadh 11451, Saudi Arabia

[2] Department for Chemistry, College of Sciences, King Saud University, Riyadh 11451, Saudi Arabia

In the recent decade, semiconductor materials are the most extensively used substances owing to their unique electrical, magnetic, conducting, and optical properties [1–3, 5, 6, 10, 14, 16]. Because of these physiochemical features, they open various avenues in applied sciences such as gas sensors, biosensors, supercapacitors, lithium-ion batteries, solid fuel cells, hydrogen/water splitting, solar cells, photocatalysts, and catalysts [17]. Outstanding specific characteristics of semiconductor materials give exceptional prospects for interfacing electronic signal transduction with chemical/biological identification measures and for the creation of a new generation of bioelectronic procedures that could demonstrate unusual utilities. These materials also have large specific surface area per unit mass, and particles are on the nanometer scale showing novel physiochemical characteristics. As the dimension of the substance reduces, the real surface area, as well as the surface-to-volume ratio, increases significantly. Scale and geometry also influence the passage of electrons and holes in semiconductor nanomaterials. In literature, several semiconductor metal oxides such as ZnO, ZrO_2, CeO_2, SnO_2, TiO_2, V_2O_5, and Fe_3O_4 have been successfully applied in various applications such as spintronic, photocatalysts, catalysts, solar cells, sensors, supercapacitors, and fuel cells [17]. Based on the crystal structure and physiochemical properties, these semiconductor metal oxides revealed electrical, optical, conducting, and catalytic properties. So the selection of the appropriate semiconductor metal oxide plays a crucial role to target the particular application.

Among them, cerium oxide (CeO_2) is considered a semiconductor metal oxide and is widely valued for its extensive use in solid electrolytes, solar cells, photocatalysts, catalysts, fuel cells, electrochemical O_2 pumps, sensors, UV/visible and luminescent materials, O_2 loading ability, NOx reduction, and amperometric O_2 ion performance due to its high conductivity of oxygen ions arising from Ce metal variable oxidation states (+3 and +4) [18, 19]. CeO_2 can support the variations in its stoichiometry to preserve a fluorite structure owing to its electronic crystal structure design. Due to its outstanding photophysical characteristics, such as a cubic fluorite crystalline phase, transparent in UV/visible range, redox reversible Ce^{4+}/Ce^{3+} cycles, steadiness within a wider range of temperatures and pressures, and extraordinary O_2 storage/release capability, ceria have been used as a potential electrocatalyst in recent years [20–22]. The high oxygen ion mobility or oxygen storage/release capacity enhances the redox performance of the CeO_2 material [23, 24]. Recently, CeO_2 was successfully used as a necessary electrocatalytic material for the detection of various analytes or oxidation of automobile gases. To this point, its electrocatalytic efficiency depends primarily on redox activity and its high capacity to store O_2 species. Their O_2 storage potential can be altered by changes in the crystal phase such as stoichiometry, surface defect evolution, O_2 species mismatch, the introduction of reactive sides, and substitution of metal impurities [24, 25]. These are the most significant factors that maximize the electrocatalytic efficiency of the crystal lattice of CeO_2. One effective way to boost the efficiency of the host materials is by doping CeO_2 with an excellent conductive metal [23, 25]. Substitution of transition metal ions into CeO_2 crystal lattice could improve the ionic mobility as well as the electrocatalytic activity in comparison to bulk pure CeO_2 material conductivity [19, 23, 25, 26]. Among the transition metal ions, doping of Mn ion is unique because of its variable oxidation states (+2, +3, +4, +6, and +7), which creates a synergistic effect among the ionic pairs of $Mn^{2+}/Mn^{3+}/Mn^{4+}$ and Ce^{3+}/Ce^{4+} leading to larger interfacial redox performance [20, 22].

Here, manganese-doped cerium oxide nanoparticles (CeO_2:Mn NPs) were effectively synthesized by the polyol-based co-precipitation route. As-synthesized nanoproduct was characterized by X-ray diffraction (XRD), transmission electron microscopy (TEM), energy-dispersive X-ray (EDX) analysis, and UV/visible absorption spectra to investigate the phase purity, crystal phase, morphology, chemical composition, and optical properties of the nanoproduct. Several researchers have observed that the high capacity for Mn impurity causes crystallographic, morphological structure, electronic, and optical properties in CeO_2. Consequently, this research pursues to improve the electrocatalytic performance of the CeO_2:Mn NPs. Cyclic voltammetry (CV) and electrochemical impedance spectroscopic (EIS) techniques were used to explore the electrocatalytic properties of the as-prepared NPs. An electrode was constructed by deposition of CeO_2:Mn NPs on a glassy carbon electrode (GCE) and monitored the electrochemical performance in 10 pH phosphate buffer solution (PBS).

Experimental

Materials

$Ce(NO_3)_3{\cdot}6H_2O$ (99.9, BDH Chemicals, UK), manganese nitrate (E-Merck, Germany), NH_4OH, and ethylene glycol were employed as preliminary materials for synthesis deprived of further distillation. Milli-Q (Millipore, Bedford, MA, USA) water was utilized for the preparation and characterization of the nanomaterials.

Synthesis

Briefly, 9.3 ml of 2 M cerium nitrate (2 M) and 0.7 ml 2 M manganese nitrate (2 M) freshly prepared solution were mixed in 100 ml Milli-Q water with constant stirring on a hot plate at 80 °C. Later on, equivalent ethylene glycol

was introduced in the mixture for complexation with metal nitrate [3, 10, 11, 27]. This reaction was proceeding on the hotplate with mechanical stirring for the formation of a completely homogeneous solution. In this homogeneous hot solution, ammonium hydroxide solution was introduced dropwise for hydrolysis to get precipitation. Occurred precipitate was extracted by centrifugation and washed numerous times with Milli-Q H_2O to eliminate unreacted reactants and surface-anchored organic moieties. This product was dried out in an oven at 100 °C and later annealed in a furnace up to 400 °C for 2 h for a complete transformation into CeO_2:Mn NPs. The obtained product was used for further characterization.

Characterization

X-ray diffraction pattern (XRD, Rigaku-Dmax-2500 Cu, Kα, radiation $\lambda = 1.5406$ Å) was utilized to analyze the phase purity and crystal phase of the nanoproduct. Field emission transmission electron microscopy (FE-TEM, JEM-2100F, JEOL, Japan) is equipped with energy-dispersive X-ray (EDX) analysis operating at an accelerating voltage of 200 kV. UV/visible spectrum was measured from a UV/visible spectrophotometer (Carry-200, Agilent Technologies, USA) in the 200–700-nm wavelength range. Electrochemical properties and sensing performance were observed (PGDTAT30, Metrohm Autolab, Switzerland). The three electrodes are attached to the electrochemical analyzer to develop the sensor to complete the cell circuit in which the glassy carbon electrode (GCE) functions as a working electrode, Ag/AgCl (saturated KCl) acts as a reference, and the counter electrode is the Pt foil. The electrodes of CeO_2:Mn NPs were processed under ambient conditions and were not stored in a cooled or neutral atmosphere until measuring the CV and EIS results. The sample surface was made by mixing a small amount of NPs with electrical insulation nature butyl carbitol acetate at an 80–20 molar ratio, then depositing the mixture onto the GCE and drying it at 60 °C for 30–45 min to achieve a uniform coating over the excellent surface of the electrode with an effective surface area of 0.07 cm^2. All of these electrochemical tests were carried out at room temperature.

Results and discussion

Crystallographic and morphological studies

The X-ray diffraction pattern was performed to investigate the formation of a single-phase, highly phase purified nanocrystalline product. Figure 1 displays most of the main characteristic diffraction planes consigned to (111), (200), (220), (311), and (222) which are well-suited with

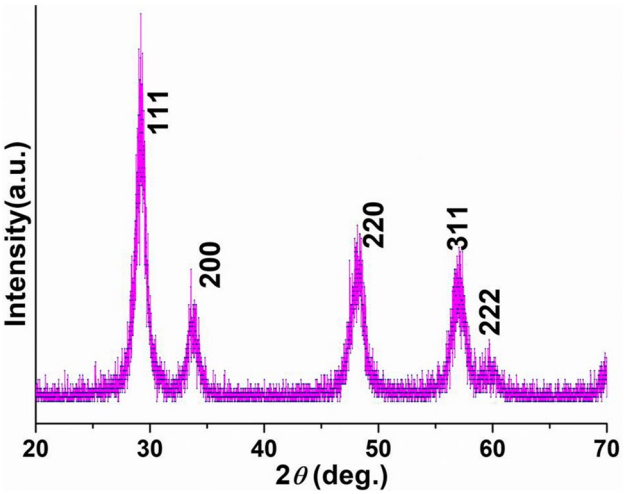

Fig. 1 X-ray diffraction pattern of CeO_2:Mn NPs

the pure phase of cubic fluorite phase of CeO_2 (space group: *Fm3m*) [11, 13, 28–30]. No diffraction plane related to manganese oxide was observed that it shows the formation of single-phase CeO_2 nanoproduct or homogeneous mixing of manganese ions in the crystal matrix. The diffraction pattern exhibited broadening in peak width; it represents the nanocrystalline nature of the as-synthesized nanoproduct. The grain dimension of the as-synthesized nanoproduct was estimated from the Debye–Scherrer formula by the most dominant reflection plan (111) observed at 2θ value 29.15 that is to be 10 nm [31–33].

To determine the morphological structure of the as-synthesized nanoproduct, high-resolution transmission electron microscopy (TEM) was performed. The shape and size of the sample were analyzed from TEM micrographs as presented in Fig. 2. An obtained nanoproduct morphology indicates a polycrystalline nature, an irregular spherical shape, rough surface, narrowly distributed, and sizes ranging from 9 to 10 nm, which is in accord with the XRD data obtained (Fig. 2a). As shown in TEM pictures, the NPs that are aggregated may be due to their high hydrophilicity with aqueous media. Because the nanoproduct was prepared in aqueous media and may be a little amount still attached over the nanoparticle surface and for TEM micrographs, the solution was prepared in aqueous media for dropping on a carbon-coated copper grid, resulting from small grain size NPs close to each other and aggregated, causing hydrogen bonding formation and electrostatic interaction. These qualitative results indicate that the obtained particles are in nanocrystallites. Besides, we conducted selected area electron diffraction (SAED) analysis through an FE-TEM instrument to see the crystal phase, nanocrystalline, and crystallography of the as-synthesized nanoproduct. As demonstrated in Fig. 2b–d, most of the observed lattice fringes are at spaces of around

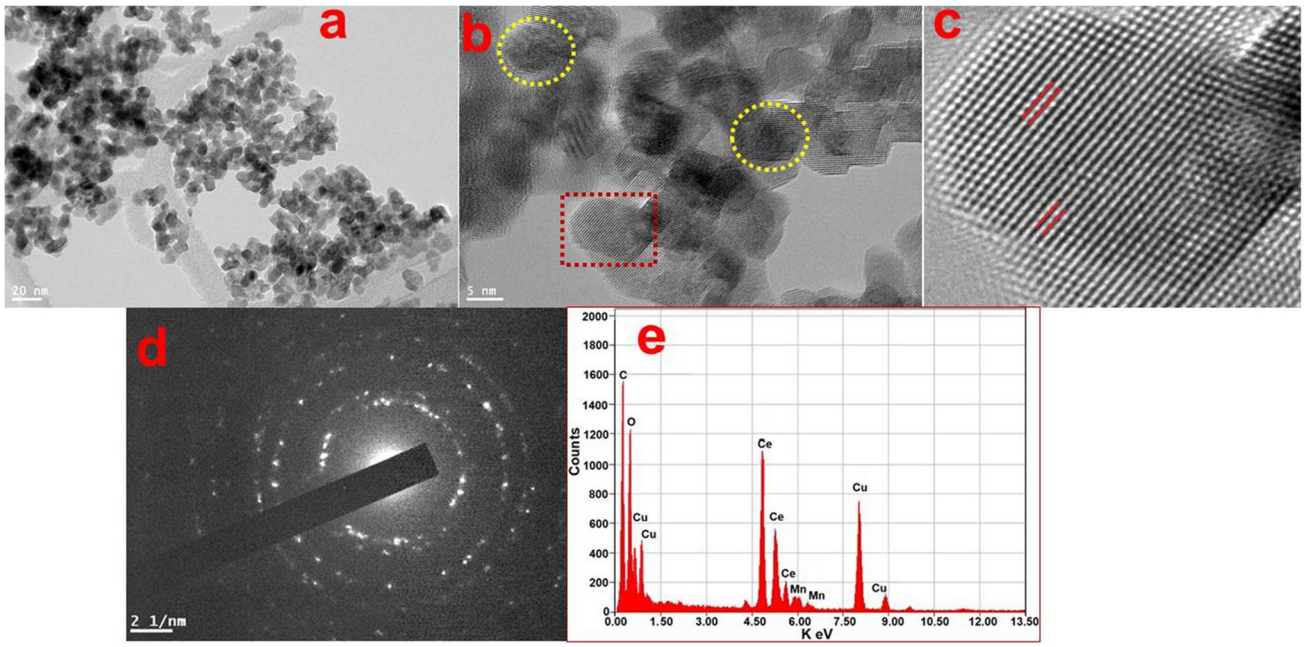

Fig. 2 Field emission transmission electron microscopic images: (**a**) low-resolution FE-TEM image, (**b**) high magnifying image, (**c**) high magnifying lattice fringes, (**d**) selected area electron diffraction pattern, and (**e**) EDX analysis of the as-prepared CeO_2:Mn NPs

0.3 nm that are assigned well to the (111) lattice plane of a cubic phase identical to fluorite. The SAED in Fig. 2d illustrates the four wide-ranging rings with excellent d-spacing, attributable to the (111), (200), (220), and (311) diffraction lines of cubic fluorite structure [21, 31–33]. Furthermore, TEM micrographs are also in use in various parts of the nanoproduct section to examine the occurrence of any Mn oxide–related minor phase in Mn-doped CeO_2 NPs. An expansion in diffraction rings indicates the small size of the particle or nanocrystalline, which is in accord with the XRD observations. Energy-dispersive X-ray (EDX) analysis was utilized to determine the chemical constituents of the nanoproducts. As observed in Fig. 2e, the EDX spectrum revealed all expected signals related to cerium (Ce), manganese (Mn), and oxygen (O), which specified the construction of a single-phase nanoproduct with high purity. There are no other peaks observed related to any other contamination, which exhibited the high phase purity of the nanoproduct. Two lines of C and Cu were also observed which are from the carbon-coated copper grid (substrate).

Optical spectra

UV/visible spectrum was observed to determine the optical properties of the CeO_2:Mn NPs. Figure 3 demonstrates the optical absorption spectrum of the sample. The spectrum demonstrated broadband with peak maxima at 331 nm, because of charge transfer transition from $O_2(2p)$ to $Ce^{4+}(4f)$ sub-shell in CeO_2, which is close to the bulk counterpart (Fig. 3a) [11, 28, 29, 34]. Bandgap energy (E_g) was considered from the absorption spectrum of CeO_2:Mn NPs. An optical bandgap value was determined by suitable absorption data by generalizing the linear part of the curves to zero absorption to the direct transfer equation. Figure 3b presents the spectrum employed for the estimation of bandgap energy to be 3.27 eV. Similar bandgap energy values were observed by various researchers [35], such as Yue and Zhang who observed that Co doping in CeO_2 lattice could more efficiently minimize the CeO_2 bandgap than other transition metal dopants [36, 37]. Masui et al. observed 3.38 and 3.44 eV bandgaps for CeO_2 NPs prepared by a reverse micelle process [38]. So the substitution of Co ions into CeO_2 crystals produces O_2 species and prefers Ce^{3+} from Ce^{4+} formation. This upsurges the number of Ce states, contributing to the creation of confined energy states that are nearby to the band of conduction, thus reducing the difference in the band [39]. It is well-accepted that CeO_2 is a redox-active semiconductor material and variation in the energy bandgap has additional importance in the creation of oxygen vacancies. These oxygen species are highly applicable in charge transfer resulting in improved electrocatalytic performance of electrodes, which are usable in photo-catalytic, supercapacitor, and electrochemical biosensing applications.

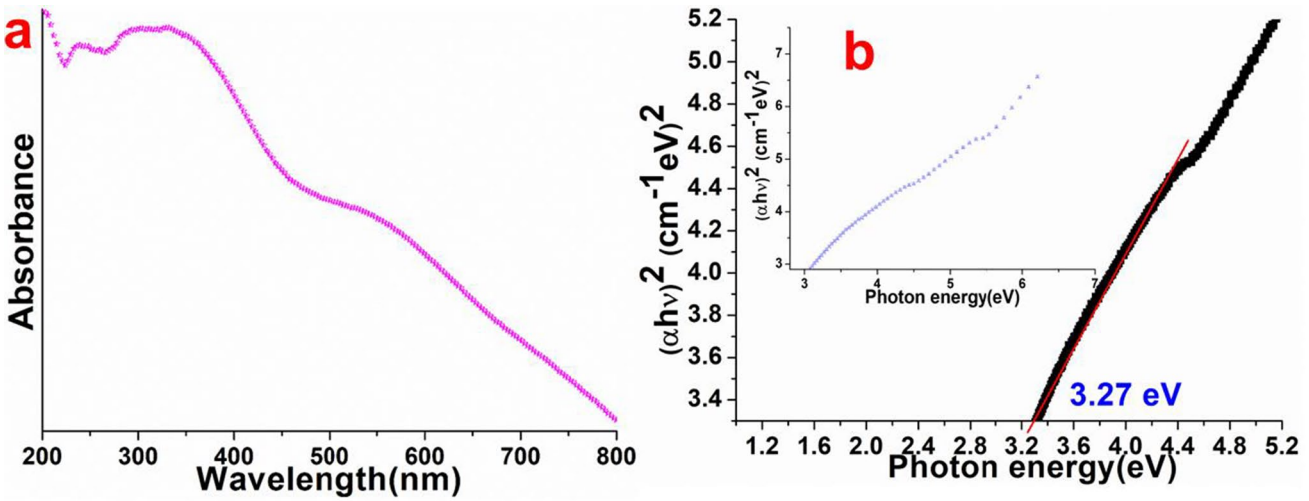

Fig. 3 (**a**) UV/Vis absorption spectrum of CeO_2:Mn NPs and (**b**) energy bandgap, photon energy ($h\nu$) vs $(\alpha h\nu)^2$

Electrochemical characterization

The cyclic voltammetry technique was performed to assess the electrochemical properties of the nanoproducts. The CeO_2:Mn NPs were pasted on GCE to measure the electrochemical behavior of the fabricated electrode. As shown in Fig. 4a, the current was observed of the blank electrode in 100 ml 0.1 M phosphate buffer solution (PBS) at 7.2 pH with a 100 mV/s scan rate. After that, the electrode surface was modified with CeO_2:Mn NPs to measure the current. In the obtained spectrum, no prominent peak was observed, from which it is clear that no redox reaction occurred, and that there was no potential on the bare electrode. After modification of the electrode surface with CeO_2:Mn NPs, a small hump appeared that may be due to the high electrocatalytic property of the CeO_2:Mn NPs. Whereas, on measuring the electrode current in the presence of urea solution in similar conditions, the oxidation peak current remarkably increased. It illustrates that the modified electrode efficiently electrochemically catalyzes the analyte. Furthermore, it is a fact that ceria have a reversible oxidation state, so it gives good redox performance, but on the addition of Mn ions in the ceria lattice, it improved the electrocatalytic activity of the materials, resulting in the fabricated electrode to show high peak current as shown in Fig. 4a. Figure 4b displays the CV current response at different potential scan rates from 5 to 150 mV/s. As shown in Fig. 4b, c, the magnitude of peak current increased linearly as the potential scan rate was increasing in similar conditions. A gradual change in peak current on changing the potential rate as shown in Fig. 4c exhibited the relationship between current and potential and charge transfer kinetic over the exterior of the constructed electrode. The linear change in the peak current reflects the redox reaction in a diffused-controlled system [3, 9, 11, 16]. The linear plots for the anode's ionization potential (IPa) and the cathode's ionization potential (IPc) for the evaluation of correlation coefficients were also generated based on the regression coefficient results (R^2). As illustrated in Fig. 4c, the IPa had an R^2 of 0.9832, whereas IPc had an R^2 of 0.9742, respectively.

Electrocatalytic activity as a function of concentration

The sensing performance of the constructed CeO_2:Mn NPs/GCE electrode was monitored as a function of urea concentration through cyclic voltammetry in 7.2 pH, 0.1 M 100 PBS at a 100 mV/s potential scan rate. The urea sensing is carried out using an electrochemical CV technique in which the current or current flow produced at the working electrode is observed concerning the counter electrode. During the experiments, a reference electrode potential is kept constant for the operating electrode. The CV phenomenon of the CeO_2:Mn/GCE electrode is seen in Fig. 5 as a purpose of the 100 mV/s urea quantity in a 1.0 mM PBS. As revealed in Fig. 5, the current magnitude is gradually increased by adding the concentration of urea from its lower to a higher concentration. The inset of Fig. 5 shows that the high-resolution graph of the oxidative peak current on accelerating the urea concentration peak current was modified successively. The fabricated CeO_2:Mn/GCE electrode, with a sensitivity of 2.82 µA mM^{-1} cm^{-2} and a regression coefficient (r^2) of 0.9862, has good linearity in the urea concentration range of 3.90–1000 mg/dl.

Moreover, with the rise in urea concentration, the linearity changed in oxidation peaks, which is strong evidence to advocate that the fabricated Mn-doped CeO_2 electrode effectively electro-catalyzes the urea concentration. It showed that, because of the diffusion-controlled mechanism, the

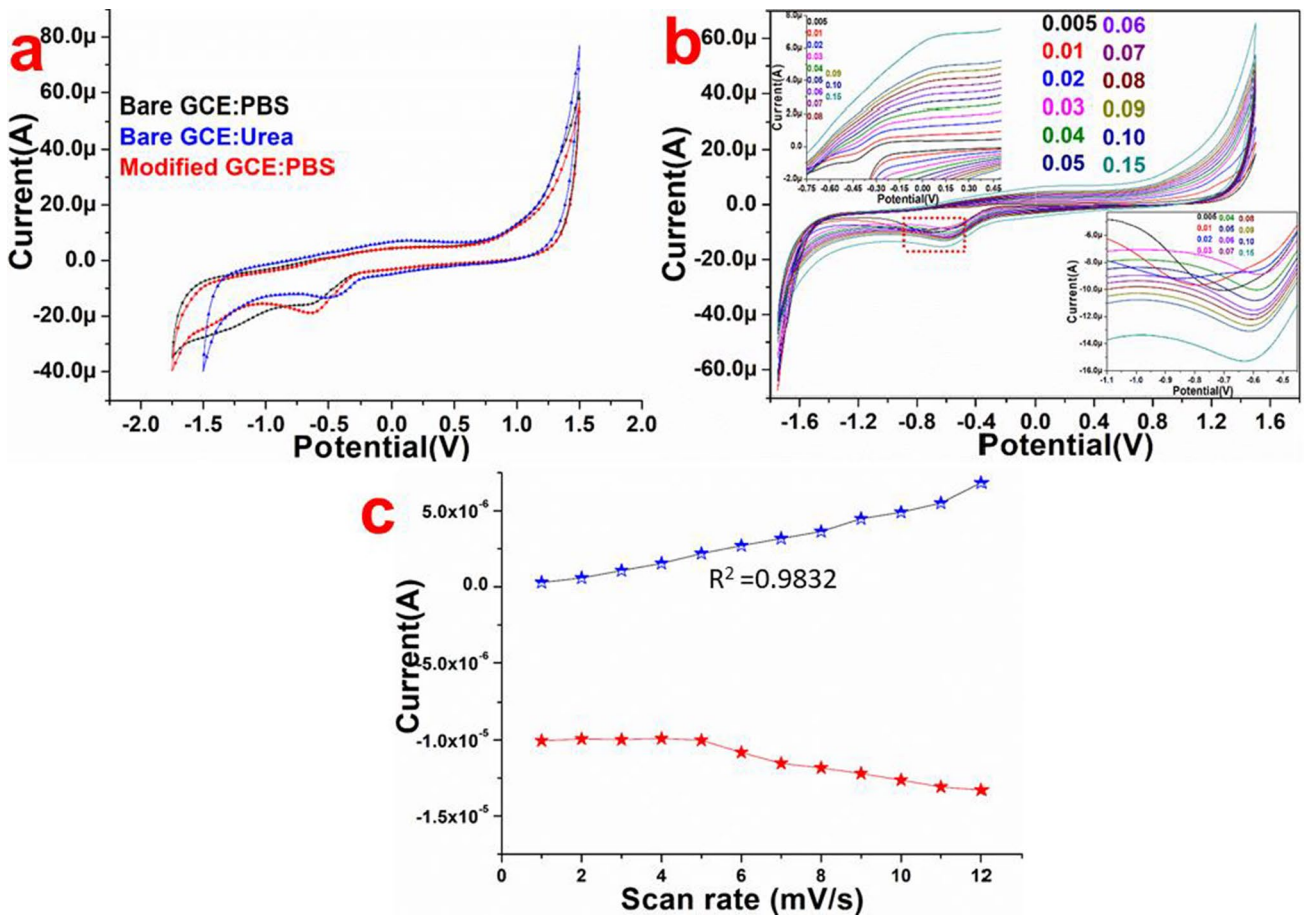

Fig. 4 (**a**) Cyclic voltammogram of bare and modified electrodes in the absence and presence of urea (500 µM) in 0.01 M PBS (pH 7.4) at 100 mVs^{-1} scan rate. (**b**, **c**) CV of CeO_2:Mn/GCE electrode as a function of scan rate (5, 10, 20, 30, 40, 50, 60, 70, 80, 90, 100, and 150 mV/s) in ascending order in PBS

CeO_2:Mn/GCE electrode successfully electro-catalyzes the urea concentration.

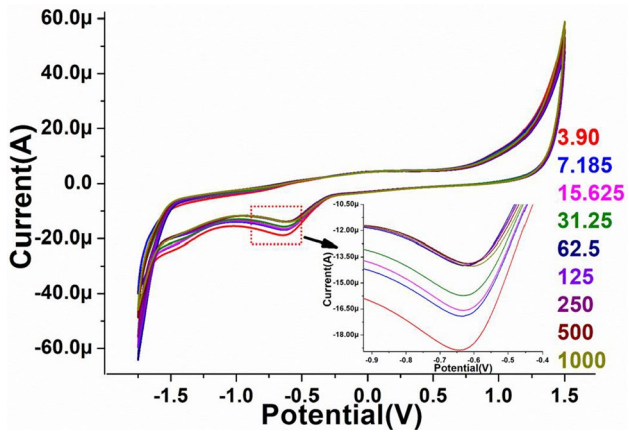

Fig. 5 Electrochemical performance of CeO_2:Mn/GCE electrode at different concentrations of urea in 0.01 M PBS

Electrochemical impedance spectroscopy (EIS) was applied to further validate the electrocatalytic activity of the fabricated electrode. EIS is an effective technique to measure the electron transfer process over the exterior of the constructed electrode through resistance. It is considered that the EIS is subjected from higher to lower frequency areas, respectively [8, 16]. The diameter of the semicircle curve indicates that the electron transfer resistance at the electrode interface is equal to the electron transfer kinetics of the designed redox probe. As seen in Fig. 6, a high interfacial Rct is seen by the broader semicircle curve, arising from the low electrical conductivity of the active material. As illustrated in Fig. 6, on increasing concentration ranges of the urea, the diameter of the semicircle is varied; it indicates the strong electrocatalytic performance in the presence of the fabricated ceria electrode. These findings in the form of curves demonstrate that the semicircle diameter is initiated at low urea concentration and large size is specifically correlated with higher concentrations, which could be attributed to high

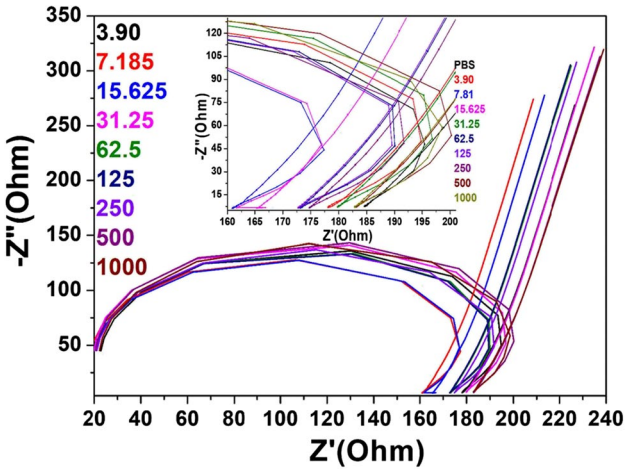

Fig. 6 Electrochemical impedance spectroscopy performance of CeO_2:Mn/GCE electrode at different concentrations of urea in 0.01 M PBS

CeO_2:Mn/GCE electrode Rct values. The diameter of the semicircles increases with the increase of the attribute of urea concentration that the Rct value is comparable and directly proportional to the urea concentrations and that is why the active high catalytic properties are demonstrated by the CeO_2:Mn. These findings are in good agreement with the above cyclic voltammetry results.

Reproducibility/stability

Electrochemical stability and reproducibility of the observed results are important parameters for the developed sensing electrode. To determine the steadiness and reproducibility, the fabricated electrode was multi-scan (nine consecutive cycles) at a constant potential. As exhibited in Fig. 7a, the fabricated electrode illustrated excellent stability in the presence of urea in PBS. It induced that the constructed electrode efficiently reproduced the sensing results and represents high stability in PBS. The prepared electrochemical sensor was kept at ambient conditions during which a slight change in the current of the voltammetric cycle was observed, confirming again the long-term stability of the constructed electrode (Fig. 7b). The findings suggest that the CeO_2:Mn/GCE sensing electrode is extremely stable with good reproducibility and that it is long-term durable and thus acceptable for the detection of pathogenic or hazardous chemicals (analytes).

Conclusion

Polycrystalline CeO_2:Mn NPs prepared by the polyol-assisted co-precipitation process were successfully applied to electrochemically catalyze urea or for urea detection. XRD results verified the single-phase, polycrystalline, nanocrystals with an average grain size of ~ 10 nm. TEM micrographs validated the grain size is small, has irregular spherical shape, and narrow size distributed with a rough surface. EDX analysis confirmed the doping of Mn ions in CeO_2 crystal lattice, which was homogeneously distributed. The optical absorption spectrum and bandgap energy were estimated to verify the phase formation and optical properties. The cyclic voltammetry studies were tested to examine the electrocatalytic characteristics and stability of the as-fabricated electrode. The electrocatalytic activity of the CeO_2:Mn/GCE was evaluated at environmental conditions in 7.2 pH, 0.1 M 100 ml PBS with the urea concentration range from 3.90 to 1000 mg/dl mixed solution. The CV and EIS techniques confirmed that the fabricated electrode efficiently electro-catalyzed the urea concentration of the

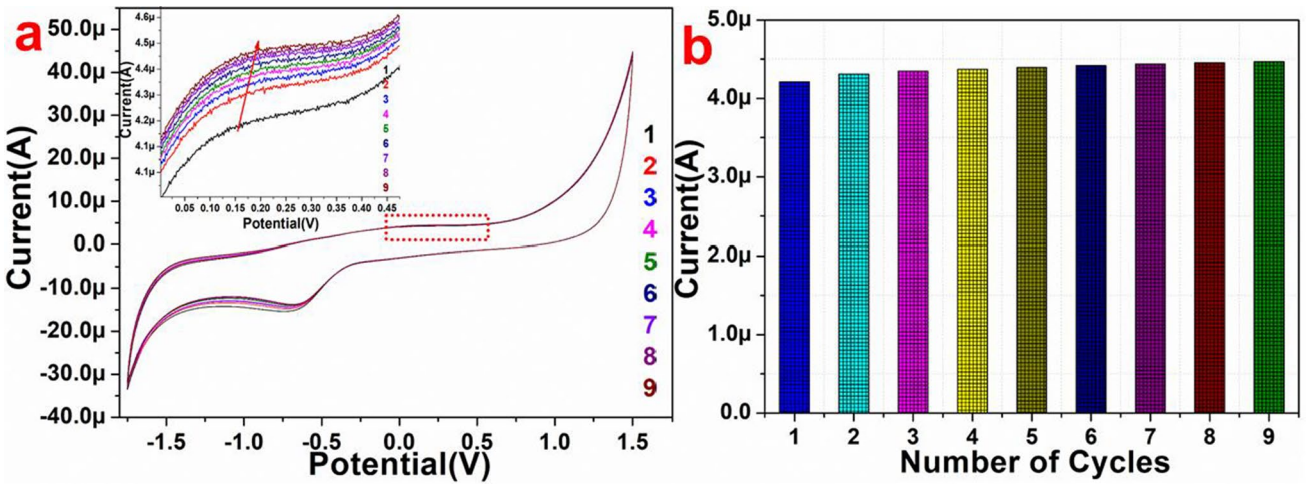

Fig. 7 (**a**, **b**) Electrochemical stability measured by CV at nine consecutive cycles of CeO_2:Mn/GCE electrode in the presence of 500 µM (urea) in 0.01 M PBS at 100 mV/s

observed concentration range. The CeO_2:Mn absorbs H_2O_2 by exchanging the electrons and facilitates in organizing the electrochemical reaction. The CV and EIS observed results endorse the high electrocatalytic activity of the as-fabricated polycrystalline CeO_2:Mn/GCE electrode. The observed cyclic voltammetry profile revealed that the current rate is higher in the presence of urea in the solution than in the absence of urea in the solution, indicating that modified CeO_2:Mn/GCE may work at a wide range of potentials. These findings carry substantial information and clear evidence of the role of Ce^{3+}/Ce^{4+} as well as doping on Mn ion cations in CeO_2 crystal lattice subsequent in expanding electrocatalytic sensing performance of the electrode.

Author contribution Anees A. Ansari: conceptualization, methodology, investigation, resources, data curation, writing—original draft, writing—review and editing, supervision, project administration, funding acquisition. Manawwer Alam: methodology, validation, formal analysis, data curation.

Funding The authors extend their appreciation to the Researchers Supporting Project (grant no. RSP-2021/365), King Saud University, Riyadh, Saud Arabia, for financial support.

Declarations

Conflict of interest The authors declare no competing interests.

References

1. Solanki, P.R., Kaushik, A., Ansari, A.A., Sumana, G., Malhotra, B.D.: Zinc oxide-chitosan nanobiocomposite for urea sensor. Appl. Phys. Lett. **93**(16) (2008). https://doi.org/10.1063/1.2980448Artn163903
2. Kaushik, A., Solanki, P.R., Ansari, A.A., Ahmad, S., Malhotra, B.D.: Chitosan-iron oxide nanobiocomposite based immunosensor for ochratoxin-A. Electrochem. Commun. **10**(9), 1364–1368 (2008). https://doi.org/10.1016/j.elecom.2008.07.007
3. Ansari, A.A., Solanki, P.R., Malhotra, B.D.: Sol-gel derived nanostructured cerium oxide film for glucose sensor. Appl. Phys. Lett. **92**(26) (2008). https://doi.org/10.1063/1.2953686Artn263901
4. Khan, R., Kaushik, A., Solanki, P.R., Ansari, A.A., Pandey, M.K., Malhotra, B.D.: Zinc oxide nanoparticles-chitosan composite film for cholesterol biosensor. Anal. Chim. Acta **616**(2), 207–213 (2008). https://doi.org/10.1016/j.aca.2008.04.010
5. Ali, A., Ansari, A.A., Kaushik, A., Solanki, P.R., Barik, A., Pandey, M.K., Malhotra, B.D.: Nanostructured zinc oxide film for urea sensor. Mater. Lett. **63**(28), 2473–2475 (2009). https://doi.org/10.1016/j.matlet.2009.08.038
6. Kaushik, A., Solanki, P.R., Ansari, A.A., Malhotra, B.D., Ahmad, S.: Iron oxide-chitosan hybrid nanobiocomposite based nucleic acid sensor for pyrethroid detection. Biochem. Eng. J. **46**(2), 132–140 (2009). https://doi.org/10.1016/j.bej.2009.04.021
7. Ansari, A.A., Singh, R., Sumana, G., Malhotra, B.D.: Sol-gel derived nano-structured zinc oxide film for sexually transmitted disease sensor. Analyst **134**(5), 997–1002 (2009). https://doi.org/10.1039/b817562d
8. Ansari, A.A., Kaushik, A., Solanki, P.R., Malhotra, B.D.: Nanostructured zinc oxide platform for mycotoxin detection. Bioelectrochemistry **77**(2), 75–81 (2010). https://doi.org/10.1016/j.bioelechem.2009.06.014
9. Ansari, A.A., Solanki, P.R., Malhotra, B.D.: Hydrogen peroxide sensor based on horseradish peroxidase immobilized nanostructured cerium oxide film. J. Biotechnol. **142**(2), 179–184 (2009). https://doi.org/10.1016/j.jbiotec.2009.04.005
10. Ansari, A.A., Sumana, G., Pandey, M.K., Malhotra, B.D.: Sol-gel-derived titanium oxide-cerium oxide biocompatible nanocomposite film for urea sensor. J. Mater. Res. **24**(5), 1667–1673 (2009). https://doi.org/10.1557/Jmr.2009.0212
11. Ansari, A.A., Kaushik, A., Solanki, P.R., Malhotra, B.D.: Sol-gel derived nanoporous cerium oxide film for application to cholesterol biosensor. Electrochem. Commun. **10**(9), 1246–1249 (2008). https://doi.org/10.1016/j.elecom.2008.06.003
12. Ansari, A.A., Sumana, G., Khan, R., Malhotra, B.D.: Polyaniline-cerium oxide nanocomposite for hydrogen peroxide sensor. J. Nanosci. Nanotechnol. **9**(8), 4679–4685 (2009). https://doi.org/10.1166/jnn.2009.1085
13. Kaushik, A., Solanki, P.R., Ansari, A.A., Ahmad, S., Malhotra, B.D.: A nanostructured cerium oxide film-based immunosensor for mycotoxin detection. Nanotechnology **20**(5) (2009). Artn 05510510.1088/0957–4484/20/5/055105
14. Ansari, A.A., Solanki, P.R., Malhotra, B.D.: Sol-gel derived nanostructured tin oxide film for glucose sensor. Sens. Lett. **7**(1), 64–71 (2009). https://doi.org/10.1166/sl.2009.1011
15. Solanki, P.R., Kaushik, A., Ansari, A.A., Sumana, G., Malhotra, B.D.: Horse radish peroxidase immobilized polyaniline for hydrogen peroxide sensor. Polym. Adv. Technol. **22**(6), 903–908 (2011). https://doi.org/10.1002/pat.1594
16. Ansari, A.A., Kaushik, A., Solanki, P.R., Malhotra, B.D.: Electrochemical cholesterol sensor based on tin oxide-chitosan nanobiocomposite film. Electroanalysis **21**(8), 965–972 (2009). https://doi.org/10.1002/elan.200804499
17. Chen, X., Dong, B., Islam, Q.A., Song, H., Wu, Y.: Semiconductor-ionic properties and device performance of heterogeneous La-doped CeO2-ZnO nanocomposites. Int. J. Hydrogen Energy **46**(15), 9968–9975 (2021). https://doi.org/10.1016/j.ijhydene.2020.04.174
18. Habib, I.Y., Burhan, J., Jaladi, F., Lim, C.M., Usman, A., Kumara, N.T.R.N., Tsang, S.C.E., Mahadi, A.H.: Effect of Cr doping in CeO2 nanostructures on photocatalysis and H2O2 assisted methylene blue dye degradation. Catal. Today (2020). https://doi.org/10.1016/j.cattod.2020.04.008
19. Zheng, X., Li, Y., Liang, S., Yao, Z., Zheng, Y., Shen, L., Xiao, Y., Zhang, Y., Au, C., Jiang, L.: Promoting effect of Cu-doping on catalytic activity and SO2 resistance of porous CeO2 nanorods for H2S selective oxidation. J. Catal. **389**, 382–399 (2020). https://doi.org/10.1016/j.jcat.2020.06.010
20. Ansari, A.A., Labis, J.P., Alam, M., Ramay, S.M., Ahmad, N., Mahmood, A.: Synthesis, structural and optical properties of Mn-doped ceria nanoparticles: a promising catalytic material. Acta. Metall. Sin-Eng. Lett. **29**(3), 265–273 (2016). https://doi.org/10.1007/s40195-016-0387-0
21. Ansari, A.A., Labis, J.P., Alam, M., Ramay, S.M., Ahmed, N., Mahmood, A.: Preparation and spectroscopic, microscopic, thermogravimetric, and electrochemical characterization of silver-doped cerium(IV) oxide nanoparticles. Anal. Lett. **50**(8), 1360–1371 (2017). https://doi.org/10.1080/00032719.2016.1218499
22. Ansari, A.A., Ahmad, N., Alam, M., Adil, S.F., Ramay, S.M., Albadri, A., Ahmad, A., Al-Enizi, A.M., Alrayes, B.F., Assal, M.E., Alwarthan, A.A.: Physico-chemical properties and catalytic activity of the sol-gel prepared Ce-ion doped LaMnO3 perovskites. Scientific Reports **9** (2019). ARTN 774710.1038/s41598–019–44118–1

23. Yu, X., Wu, X., Chen, Z., Huang, Z., Jing, G.: Oxygen vacancy defect engineering in Mn-doped CeO2 nanostructures for nitrogen oxides emission abatement. Mol. Catal. **476**, 110512 (2019). https://doi.org/10.1016/j.mcat.2019.110512
24. Khakhal, H.R., Kumar, S., Dolia, S.N., Dalela, B., Vats, V.S., Hashmi, S.Z., Alvi, P.A., Kumar, S., Dalela, S.: Oxygen vacancies and F+ centre tailored room temperature ferromagnetic properties of CeO2 nanoparticles with Pr doping concentrations and annealing in hydrogen environment. J. Alloy. Compd. **844**, 156079 (2020). https://doi.org/10.1016/j.jallcom.2020.156079
25. Mousavi-Kamazani, M., Azizi, F.: Facile sonochemical synthesis of Cu doped CeO2 nanostructures as a novel dual-functional photocatalytic adsorbent. Ultrason. Sonochem. **58**, 104695 (2019). https://doi.org/10.1016/j.ultsonch.2019.104695
26. George, S.E., George, M., Alex, J., Joy, L.K., Aravind, A., Sajan, D., Thakur, A., Hussain, S., Vinitha, G.: Nonlinear optical and photocatalytic dye degradation of Co doped CeO2 nanostructures synthesized through a modified combustion technique. Ceram. Int. **46**(9), 13932–13940 (2020). https://doi.org/10.1016/j.ceramint.2020.02.189
27. Solanki, P.R., Dhand, C., Kaushik, A., Ansari, A.A., Sood, K.N., Malhotra, B.D.: Nanostructured cerium oxide film for triglyceride sensor. Sensors and Actuators B-Chemical **141**(2), 551–556 (2009). https://doi.org/10.1016/j.snb.2009.05.034
28. Ansari, A.A.: Optical and structural properties of sol–gel derived nanostructured CeO2film. J. Semicond. **31**(5), 053001 (2010). https://doi.org/10.1088/1674-4926/31/5/053001
29. Ansari, A.A., Singh, S.P., Malhotra, B.D.: Optical and structural properties of nanostructured CeO2:Tb3+ film. J. Alloy. Compd. **509**(2), 262–265 (2011). https://doi.org/10.1016/j.jallcom.2010.07.009
30. Ansari, A.A., Azahar, M., Malhotra, B.D.: Electrochemical urea biosensor based on sol-gel derived nanostructured cerium oxide. India-Japan Workshop on Biomolecular Electronics and Organic Nanotechnology for Environment Preservation **358** (2012). Artn 01200610.1088/1742–6596/358/1/012006
31. Ansari, A.A., Labis, J., Alam, M., Ramay, S.M., Ahmad, N., Mahmood, A.: Physicochemical and redox characteristics of Fe ion-doped CeO2 nanoparticles. J. Chin. Chem. Soc. **62**(10), 925–932 (2015). https://doi.org/10.1002/jccs.201500195
32. Ansari, A.A., Labis, J., Alam, M., Ramay, S.M., Ahmad, N., Mahmood, A.: Influence of copper ion doping on structural, optical and redox properties of CeO2 nanoparticles. J. Electroceram. **36**(1–4), 150–157 (2016). https://doi.org/10.1007/s10832-016-0018-1
33. Ansari, A.A., Labis, J., Alam, M., Ramay, S.M., Ahmad, N., Mahmood, A.: Effect of cobalt doping on structural, optical and redox properties cerium oxide nanoparticles. Phase Transit. **89**(3), 261–272 (2016). https://doi.org/10.1080/01411594.2015.1116532
34. Ansari, A.A., Kaushik, A.: Synthesis and optical properties of nanostructured Ce(OH)4. J. Semicond. **31**(3), 033001 (2010). https://doi.org/10.1088/1674-4926/31/3/033001
35. Saranya, J., Ranjith, K.S., Saravanan, P., Mangalaraj, D., Rajendra Kumar, R.T.: Cobalt-doped cerium oxide nanoparticles: enhanced photocatalytic activity under UV and visible light irradiation. Mater. Sci. Semicond. Process. **26**, 218–224 (2014). https://doi.org/10.1016/j.mssp.2014.03.054
36. Yue, L., Zhang, X.-M.: Structural characterization and photocatalytic behaviors of doped CeO2 nanoparticles. J. Alloy. Compd. **475**(1), 702–705 (2009). https://doi.org/10.1016/j.jallcom.2008.07.096
37. Zhang, D.-E., Zhang, X.-J., Ni, X.-M., Song, J.-M., Zheng, H.-G.: Optical and electrochemical properties of CeO2 spindles. ChemPhysChem **7**(12), 2468–2470 (2006). https://doi.org/10.1002/cphc.200600388
38. Masui, T., Fujiwara, K., Machida, K.-I., Adachi, G.-Y., Sakata, T., Mori, H.: Characterization of cerium(IV) oxide ultrafine particles prepared using reversed micelles. Chem. Mater. **9**(10), 2197–2204 (1997). https://doi.org/10.1021/cm970359v
39. Zhang, Y.-W., Si, R., Liao, C.-S., Yan, C.-H., Xiao, C.-X., Kou, Y.: Facile alcohothermal synthesis, size-dependent ultraviolet absorption, and enhanced CO conversion activity of ceria nanocrystals. J. Phys. Chem. B **107**(37), 10159–10167 (2003). https://doi.org/10.1021/jp034981o